(Received 4 November 2025, Accepted 8 December 2025, Scheduled 24 March 2026)

Complex Vector Control Based Three-Level Inverter with Centre-Tap Inductor without Direct Current

Yao He, Xiangyi Sun, Xinxin Zheng*, Xintian Liu, Yanan Zhou, and Lin He

College of Automotive and Traffic Engineering, Hefei University of Technology, Hefei 230009, China

ABSTRACT: A direct-through three-level inverter topology based on center-tap inductance and its complex vector control strategy are proposed. This topology structurally avoids the direct short-circuit problem of the DC side capacitor, eliminates the need to set a dead zone in the drive signal, and eliminates the low-order harmonics introduced by the dead zone. For this direct-through inverter, the corresponding complex vector control strategy is studied. By establishing a full-frequency domain model of the system, the fundamental cause of the coupling of DQ-axis currents in the synchronous rotating coordinate system was analyzed. To address the issue of poor dynamic response caused by coupling, a complex coefficient controller was designed. By introducing imaginary parts into the controller parameters, the additional poles introduced by the coordinate transformation were offset, thereby achieving decoupling control of the active and reactive currents. Simulated and experimental results demonstrate that, compared to the traditional real-coefficient PI controller, the proposed complex vector control strategy can effectively reduce the coupling degree of the DQ-axis current, improve the system's dynamic performance, and verify the correctness and effectiveness of the proposed topology and control method. This inverter topology features both high reliability and excellent output performance without increasing the number of power switch devices.

1. INTRODUCTION

The development of high-performance motor drive systems relies critically on the inverter as the core power conversion unit, whose performance substantially determines overall system capabilities. Multilevel inverters are finding increasing application in medium-voltage and high-power scenarios due to their enhanced output waveform quality, reduced voltage stress on switching devices, and improved electromagnetic compatibility [1–7]. By generating multi-level voltages that approximate sinusoidal waveforms, these topologies effectively reduce current harmonic distortion, thereby improving motor efficiency and minimizing torque ripple — essential requirements for high-precision motor control [8–10].

A fundamental challenge in inverter design is the risk of shoot-through. The insertion of dead time into gate signals, while being necessary to prevent DC-link capacitor short circuits caused by simultaneous conduction of upper and lower switches, introduces new complications. This measure injects low-order harmonics into the output voltage, distorts current waveforms, and, in multilevel configurations, leads to DC-link capacitor voltage imbalance. These effects manifest themselves as increased torque ripple, speed fluctuations, and reduced reliability, ultimately constraining further performance improvements.

To address these limitations, research has progressed along two primary paths. The first focuses on compensating for dead-time effects through control algorithms, primarily implemented by modifying modulation signals or switching timings. These approaches fall into two categories: modulation wave correction, which injects compensation voltages based on current polarity applicable to both SPWM and SVPWM schemes [11–13], and online estimation with adaptive compensation utilizing disturbance observers or Kalman filters for real-time dynamic adjustment [14–17]. While effectively reducing waveform distortion, these methods face inherent limitations: their performance depends on accurate system parameters that vary with temperature and operating conditions, leading to incomplete compensation; additionally, the injected compensation signals may introduce disturbances into the control system, affecting dynamic performance and stability. The computational complexity of advanced algorithms further hinders practical implementation, particularly regarding accurate current polarity detection near zero-crossings.

The second path seeks to eliminate the need for dead time entirely through topological innovation of the inverter itself. These dead-time-free topologies prevent shoot-through by incorporating inductive loops or auxiliary circuits [18–21]. While being feasible for two-level inverters, implementing such topologies in multilevel converters remains challenging without increasing cost, size, or control complexity.

In motor drive systems, conventional decoupling control strategies often demonstrate limited effectiveness in managing dynamic interactions between active and reactive currents, particularly during wide-speed-range operation, resulting in sluggish transient response and stability concerns. In comparison, Complex Vector Control reconstructs the control system in the complex frequency domain, enabling the thorough decoupling between d- and q-axis currents and significantly improving dynamic response characteristics and operational sta-

* Corresponding author: Xinxin Zheng (xinxin.zheng@hfut.edu.cn).

bility [22–26]. However, practical implementation still faces several challenges: the decoupling performance shows high sensitivity to motor parameter variations, where practical parameter drift disrupts theoretical pole-zero cancellation conditions, causing non-negligible residual coupling effects. Simultaneously, simplified models adopted to reduce implementation complexity often fail to accurately capture true system dynamics, while introducing complex observers or adaptive mechanisms inevitably increases computational burden, collectively hindering widespread engineering application [27–30].

Therefore, the integration of dead-time-free multilevel topologies with advanced Complex Vector Control represents a promising research direction. This approach, through coordinated hardware-control co-design, provides a viable pathway toward developing robust motor drive systems with high power density and superior dynamic performance.

2. TOPOLOGY AND WORKING PRINCIPLE

The topology of a single-phase inverter with a centre-tapped inductor is shown in Figure 1, where the centre-tapped output of the inductor is connected to the AC load, and the circuit does not require external or integrated anti-parallel diodes as in the conventional three-level topology due to the high voltage and high power occasions where insulated-gate bipolar transistors (IGBTs) are often used as the power switching tubes, but the diode branch composed of D_3, D_5, or D_4, and D_6 is reconstructed to achieve the inductance of the inductor. The inductor current can be avoided by reconfiguring the diode branch consisting of $D(3)$, $D(5)$, or $D(4)$, $D(6)$ to achieve the inductor current. Since the continuity current is much smaller than the current flowing through the IGBTs, D_3–D_6 can be selected as diodes with small current stress, and two series diodes can be merged into one diode to further reduce the power devices of the inverter if the diode's voltage withstand value and cost are taken into account [31].

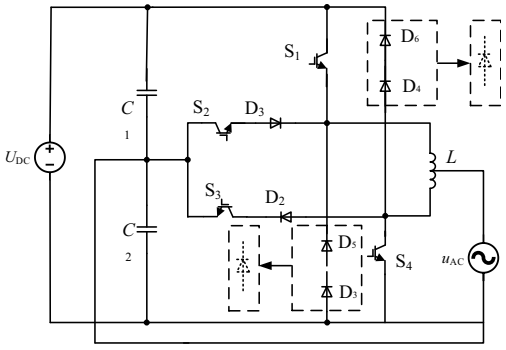

FIGURE 1. Topology of a pass-through-free single-phase inverter with centre-tap inductor.

The output modes of the inverter bridge arm are given in Figure 2, where the series diodes are merged into a single diode, to achieve a topology with three level outputs, i.e., positive level, 0 level, and negative level, corresponding to the point potentials of P, O, and N. The inductance L is divided into two parts L_1 and L_2 by the centre tap, and L always exists in a loop consisting of the power switching tubes and the capacitors on the DC side, which serves as an anti-direction effect. $Z_{(ac)}$ is the AC load, and the load voltage and current are u_{ac} and i_{ac}. The positive direction of AC voltage and current is given in the figure. When the polarity of i_{ac} is positive, L_1 acts as the filter inductor, and the output point of the bridge arm is point A. When the polarity of i_{ac} is negative, L_2 acts as the filter inductor, and the output point of the bridge arm is point B.

There are a total of four power switching tubes in the inverter, so there exist 2^4, a total of 16 switching combinations, and the switching vector $\mathbf{S}_i$ of the inverter is set as

$$\mathbf{S}_i = [S_1, S_2, S_3, S_4] \quad (i = 0, 1, \ldots, 15) \tag{1}$$

Then, there are a total of 16 switching vectors. For the switching vector $\mathbf{S}_0$, the four power switching tubes are cut off. At this time, the topology is in the diode continuation state. When the polarity of i_{ac} is positive, corresponding to Figure 2(a), the current is continued by the diode D_3, and the DC-side capacitance C_2 is charged. The output point of the bridge arm is point A, and the output voltage is $-U_{DC}/2$. At this time, the load current i_{ac} is

$$i_{ac} = i_{ac0} - \frac{U_{DC}}{2(j\omega_c L_1 + Z_{ac})} \tag{2}$$

where i_{ac0} is the initial value of the load current at the instant of $\mathbf{S}_0$ action, and i_{ac} decreases. When i_{ac} polarity is negative, corresponding to Figure 2(b), by the diode D_4 continuous current, DC side capacitor C_1 charging, the output point of the bridge arm for the B point, the output voltage is $U_{DC}/2$, and i_{ac} is

$$i_{ac} = i_{ac0} + \frac{U_{DC}}{2(j\omega_c L_2 + Z_{ac})} \tag{3}$$

Because at this time, i_{ac0} is negative, i_{ac} is still the absolute value of the decrease. It can be seen that, regardless of the polarity of i_{ac}, $\mathbf{S}_0$ effect is always to make i_{ac} the absolute value of the instantaneous value of the decrease, and $\mathbf{S}_1$, $\mathbf{S}_8$, $\mathbf{S}_9$ effect is the same as $\mathbf{S}_0$.

For the switching vector $\mathbf{S}_2$, the power tube $\mathbf{S}_3$ conducts, and when the current polarity is positive, the current does not flow through $\mathbf{S}_3$, so the topology is still in the diode renewal state of Figure 2(a). When the current polarity is negative, which corresponds to Figure 2(c), the output point of the bridge arm is point B, and the output voltage is 0. The initial value of the load current at the instant of the action of $\mathbf{S}_2$ is maintained in i_{ac}, and the effect of $\mathbf{S}_{10}$ is the same as that of $\mathbf{S}_2$. The effect of $\mathbf{S}_{10}$ is the same as that of $\mathbf{S}_2$.

For the switching vector $\mathbf{S}_3$, the power tubes $\mathbf{S}_3$ and $\mathbf{S}_4$ are on. When the current polarity is positive, it is still in the diode continuity state in Figure 2(a). When the current polarity is negative, corresponding to Figure 2(d), the capacitor C_2 is discharged; the output point of the bridge arm is point B; the output voltage is $-U_{DC}/2$. At this time, the load current i_{ac} is the expression (2). Since i_{ac0} is negative, the absolute value of $i(ac)$ increases, and the effect of $S(11)$ is the same as that of $\mathbf{S}_3$. As i_{ac0} is negative, the absolute value of i_{ac} increases, and the effect of textbfS_{11} is the same as that of $\mathbf{S}_3$.

Similarly, the corresponding effects of the 16 switching vectors can be obtained as shown in Table 1. It is worth mentioning that, for Figures 2(g), (h), and (i), the output of the bridge

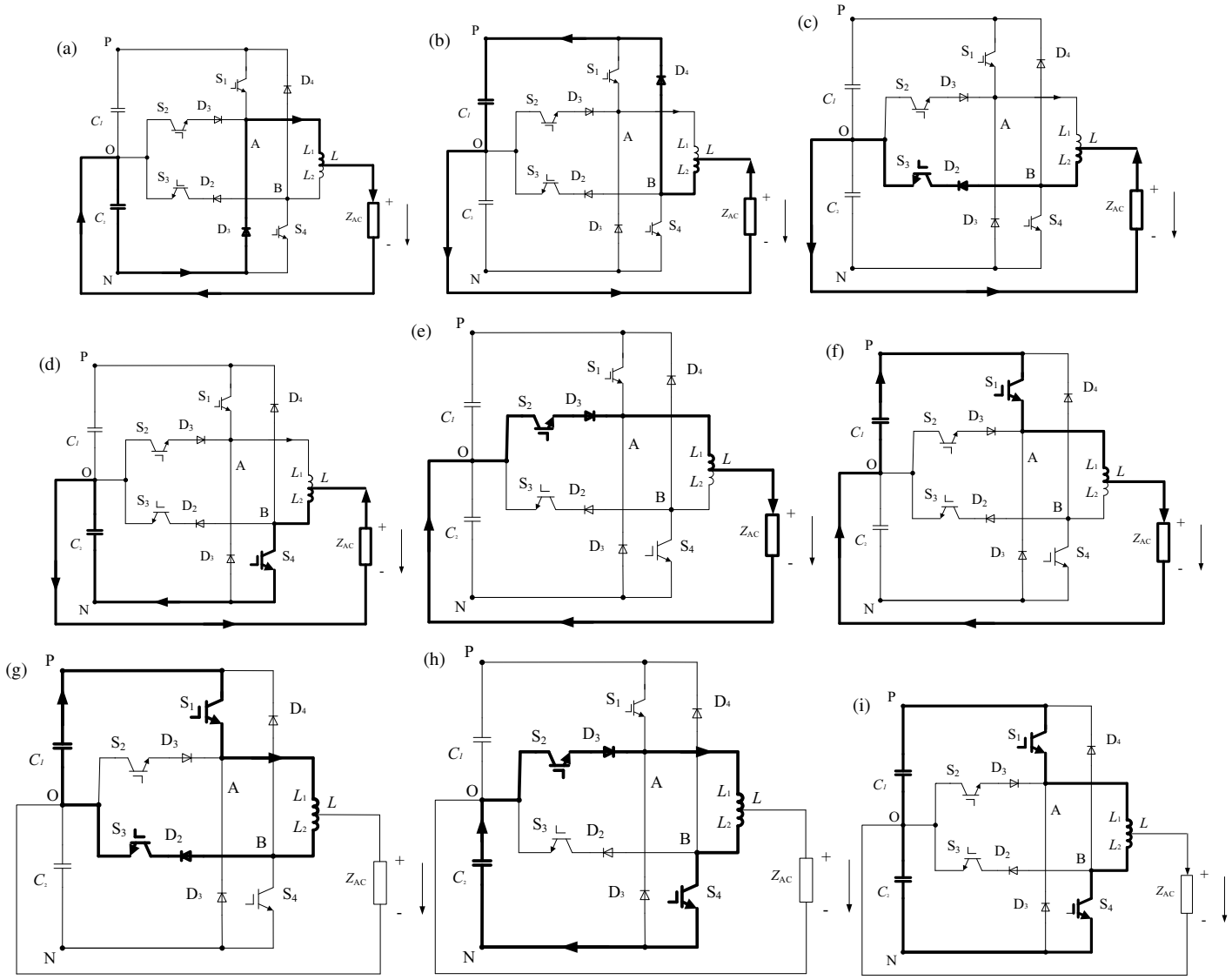

FIGURE 2. Output modes of the inverter bridge arm.

arm is unchanged regardless of the polarity of the load current, and these three modes are not allowed to appear in the conventional three-level topology because they will lead to the short-circuiting of the DC-side capacitance, whereas for the pass-through-less topology, due to the existence of the centre-tap inductance, the DC-side capacitance is not short-circuited, and the switching vectors $\mathbf{S}_{14}$ and $\mathbf{S}_7$ corresponding to Figures 2(g) and (h) are able to act as auxiliary vectors for capacitance balancing, controlling C_1 or C_2 to discharge for a short time via $\mathbf{S}_{14}$ or $\mathbf{S}_7$ when C_1 and C_2 voltages are unbalanced, which is an inherent advantage of the proposed topology in terms of balancing. For the switching vector $\mathbf{S}_{15}$ corresponding to Figure 2(i), which has no effect on the inverter output, the vector will not be actively generated in the control and will only appear passively at the moment when the power tubes are not reliably switched off, but it will not cause the risk of a pass-through; therefore, the deadband can be eliminated topologically for the proposed inverter.

3. FULL FREQUENCY DOMAIN MODELLING OF THE SYSTEM

3.1. The Influence of Coordinate Transformation

The expression for three-phase alternating current is

$$\begin{cases} i_a = I_m \cos \omega t \\ i_b = I_m \cos(\omega t - 2\pi/3) \\ i_c = I_m \cos(\omega t + 2\pi/3) \end{cases} \tag{4}$$

According to the coordinate transformation formula, its expression in the two-phase stationary coordinate system, namely the $\alpha\beta$ coordinate system, is

$$\begin{cases} i_\alpha = I_m \cos \omega t \\ i_\beta = I_m \sin \omega t \end{cases} \tag{5}$$

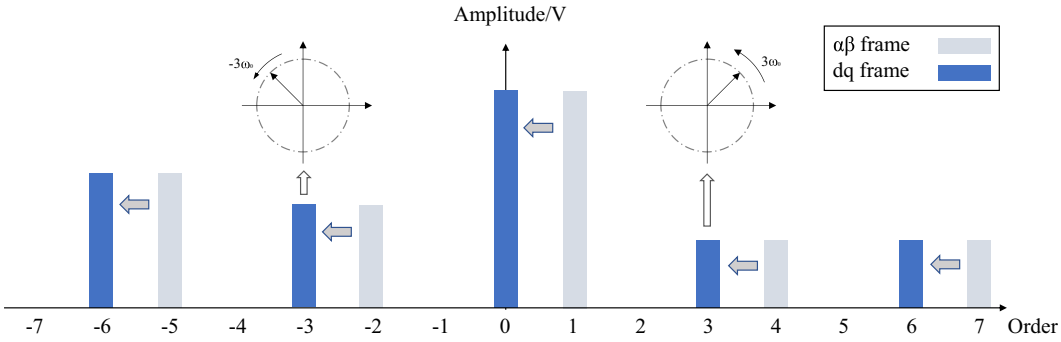

FIGURE 3. The influence of coordinate transformation on signal frequency.

The expression in the synchronous rotating coordinate system, that is, the dq coordinate system, is

$$\begin{cases} i_d = I_m(\cos\omega_0 t\cos\omega t + \sin\omega_0 t\sin\omega t) = I_m\cos(\omega-\omega_0)t \\ i_q = I_m\sin\omega_0 t\cos\omega t - I_m\cos\omega_0 t\sin\omega t = I_m\sin(\omega-\omega_0)t \end{cases} \tag{6}$$

Here, ω_0 represents the fundamental frequency. It can be seen that a coordinate transformation will cause a shift in the signal frequency. When $\omega = \omega_0$, the fundamental frequency signal corresponding to the stationary coordinate system is a DC signal in the synchronous rotating coordinate system. For AC signals of other frequencies, after coordinate transformation, the signal frequency will all shift to the left by one fundamental frequency.

Figure 3 shows the influence of coordinate transformation on signal frequency. A signal with a frequency of 1 in a stationary coordinate system is a positive sequence fundamental signal. When it is transformed to a synchronously rotating coordinate system, its frequency becomes 0, that is, a DC signal. This is the reason that a coordinate transformation can convert an AC signal into a DC signal for control. As can be seen from the figure, after all signals are transformed from the stationary coordinate system to the synchronously rotating coordinate system, their frequencies will shift to the left once. In the form of complex vectors, any signal in the stationary coordinate system can be represented as

$$\vec{u}_{\alpha\beta} = \cos\omega t + j\sin\omega t \tag{7}$$

It can be expressed in a synchronous rotating coordinate system.

$$\vec{u}_{dq} = \cos(\omega-\omega_e)t + j\sin(\omega-\omega_e)t \tag{8}$$

Equation (5) indicates that in a synchronously rotating coordinate system, an alternating current signal with a frequency of ω in the stationary coordinate system will be observed as a signal with a frequency of $\omega-\omega_0$. This characteristic causes the control system to exhibit different dynamic responses at positive sequence and negative sequence frequencies, i.e., the frequency-domain representation of the fundamental cause of asymmetry. Therefore, for any transfer function in a stationary coordinate system $G_{\alpha\beta}(s_{\alpha\beta})$, when it is transformed to a synchronously rotating coordinate system, the transfer function will become $G_{dq}(s_{dq}+j\omega_0)$.

3.2. Time-Frequency Mapping Based on Complex Vector Model

In the design of the control system, it is necessary to establish the system's transfer function and design the controller parameters in the synchronous rotating coordinate system. However, the transfer function of the inverter is established in a three-phase stationary coordinate system. After the coordinate transformation, the transfer function in the synchronous rotating coordinate system will change. It is necessary to combine the complex vector model to analyze the influence of frequency offset on the signal. In the synchronously rotating coordinate system, the transfer functions of $G_{PI}(s)$, $G_{DH}(s)$, and $G_{Fil}(s)$ are respectively

$$G_{PI}(s) = K_P + \frac{K_i}{s} \tag{9}$$

$$G_{D\&H}(s) = \frac{1}{\tau s'+1} \tag{10}$$

$$G_{Fil}(s) = \frac{1}{Ls'+R_f} \tag{11}$$

Among them, $s' = s + j\omega_0$; K_p and K_i are the proportional and integral coefficients of the PI controller; τ is the motor time constant; L is the inductance of the motor winding; and R_f is the equivalent series resistance of C_f. Based on the complex vector model of each link in the system, the complex vector model $G_{LOOP}(s+j\omega_0)$ of the entire drive motor control system can be obtained through the transfer function operation of the open-loop or closed-loop system. For the Laplacian operator s in the model, according to the mapping principle of the frequency domain, it can be replaced by the frequency domain operator $j\omega$, that is

$$G_{LOOP}(j\omega+j\omega_e) = G_{LOOP\text{-}re}(\omega,\omega_e) + jG_{LOOP\text{-}im}(\omega,\omega_e) \tag{12}$$

Among them, $G_{loop\text{-}re}$ represents the real part of G_{loop}; $G_{loop\text{-}IM}$ represents the imaginary part; and ω represents the signal frequency in the full frequency domain. When ω is negative, it represents a negative sequence AC signal; when ω is positive, it represents a positive sequence AC signal; when ω is 0, it represents a DC signal. By sweeping ω, the frequency-scale dynamic model of the system can be

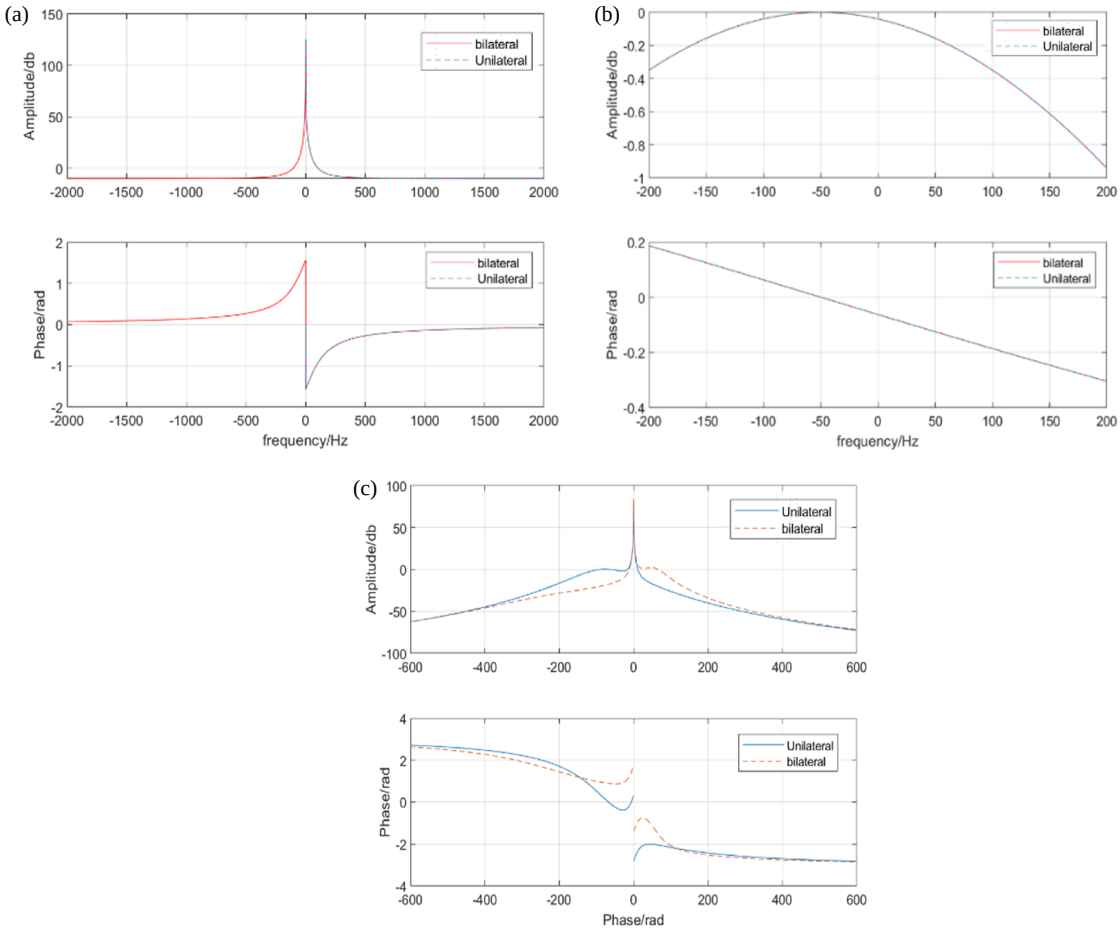

FIGURE 4. Comparison of single and double-sided frequency domain response curves. (a) PI control link. (b) PWM modulation link. (c) Filtering stage.

established.

$$\begin{cases} A_{LOOP} = \sqrt{G^2_{LOOP\text{-}re}(\omega,\omega_0) + G^2_{LOOP\text{-}im}(\omega,\omega_0)} \\ P_{LOOP} = \arctan \dfrac{G_{LOOP\text{-}im}(\omega,\omega_0)}{G_{LOOP\text{-}re}(\omega,\omega_0)} \end{cases} \tag{13}$$

Figure 4 presents the comparison of the single and bilateral frequency domain response curves of the proportional-integral (PI) control link, PWM modulation link, and single L filtering link. Among them, the solid line represents the bilateral frequency domain response curve, and the dashed line represents the unilateral frequency domain response curve. The essence of the unilateral response curve is a Bode plot, and the difference between it and the Bode plot lies in that the abscissa is not a logarithmic coordinate. The difference from the bilateral response curve lies in that no complex vector modeling is carried out, thus it cannot reflect the frequency offset caused by coordinate transformation.

For the PI control link shown in Figure 4(a), since the PI controller itself exists within the synchronous rotating coordinate system, its bilateral frequency domain response curve is completely symmetrical, and the positive frequency domain response curve coincides with the unilateral frequency domain response curve, which means that the PI controller has the same effect on positive sequence and negative sequence AC signals. For the PWM modulation link shown in Figure 4(b), the amplitude-frequency response curves of the single and bilateral sides are completely consistent, with the amplitude gain always being 0. The single-sided phase-frequency response curve passes through the origin, while the bilateral phase-frequency curve shifts to the left by 50 Hz, indicating that the coordinate transformation will introduce an additional phase lag of the fundamental frequency, which will lead to the asymmetry of the bilateral frequency-domain response curve and cause coupling of DQ-axis current. For the single L filtering link shown in Figure 4(c), the bilateral amplitude-frequency and phase-frequency response curves are both shifted to the left by one fundamental frequency. Besides the different resonant frequencies for positive and negative sequence signals, additional poles are introduced in the negative frequency domain, leading to a further reduction in the dynamic performance of the system.

4. DECOUPLING STRATEGY OF THE SYSTEM

Under the synchronous rotating coordinate system, when the transfer function has an imaginary part term, the bilateral frequency domain response curve will no longer be symmetric, so its asymmetry reflects the coupling effect of the dq-axis, and in

order to realise the decoupling, it is necessary to eliminate the imaginary part term in the transfer function through the control strategy, so as to eliminate the asymmetry of the response curve.

4.1. Decoupling of Filtering Links

According to Figure 2(c), the asymmetry of the L filter link is mainly reflected in the two resonance poles and the poles introduced by the filter inductor, which are able to be eliminated by active or passive damping although the resonance frequencies of the positive and negative sequences are different, and the bilateral frequency domain response curves of the L filter link with different passive damping are given in Figure 5. It can be seen that the larger the damping is, the less obvious the asymmetry of the two resonance poles becomes. Obviously, the additional poles introduced by the filter inductance can never be eliminated, so the decoupling of the L filter link is essentially the elimination of the poles there.

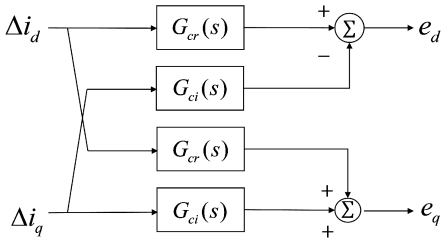

FIGURE 5. Structure diagram of complex coefficient PI controller.

The poles additionally introduced by the filter inductor can be eliminated by the complex coefficient PI controller, and the structure of the complex coefficient PI controller is given in Figure 5, in which $G_{cr}(s)$ and $G_{ci}(s)$ are the transfer functions of the real and imaginary parts of the complex coefficient PI controller, respectively, so the transfer function of the complex coefficient PI control can be expressed as

$$G_{PI}(s) = G_{cr}(s) + jG_{ci}(s) \tag{14}$$

As can be seen from Figure 5, the input signals of the controller are the current deviations Δi_d and Δi_q of the dq axis, and the output signals are ed and eq. There is a coupling relationship between the outputs of the dq axes. The complex coefficient PI controller precisely utilizes its own introduced and controllable coupling characteristics to accurately counteract the inherent coupling of the filter inductor, thereby achieving decoupling.

Considering a simplified single L filter model, its total inductance value is $L = L_1 + L_2$, and its expression in the Synchronous Reference Frame (SRF) coordinate system is

$$G_L(s) = \frac{1}{(s + j\omega_0)L + R} \tag{15}$$

From the above formula, the poles of the transfer function can be obtained, and s_p is

$$s_p = -\frac{R}{L} - j\omega_0 \tag{16}$$

Here, R is the equivalent series resistance of the inductor. According to the above formula, the frequency at the pole can be obtained as

$$\omega = -\omega_0 + j\frac{R}{L} \tag{17}$$

To cancel out this pole, there is

$$K_i = \frac{RK_p}{L} + j\omega_0 K_p \tag{18}$$

From this, the transfer functions of G_{cr} and G_{ci} can be obtained as follows

$$\begin{cases} G_{cr}(s) = K_p + \frac{RK_p}{sL} \\ G_{ci}(s) = \frac{\omega_0 K_p}{s} \end{cases} \tag{19}$$

Among them, the real part $G_{cr}(s)$ contains a proportional term and an integral term for compensating the resistive voltage drop of the inductor and providing fundamental gain. The imaginary part $G_{ci}(s)$ is a pure integrator, whose gain is proportional to the synchronization frequency, specifically designed to generate a voltage component that leads or lags by 90 degrees to counteract the back electromotive force coupling term caused by the transformation of the rotating coordinate system.

4.2. Decoupling of the PWM Modulation Link

Since the switching frequency is equal to the sampling calculation frequency, the PWM link can be modeled as a combination of a calculation delay and a zero-order retainer. According to Equation (2) and considering the effect in a synchronously rotating coordinate system, the PWM modulation link can be approximately expressed a

$$G_{PWM}(s) \approx \frac{1}{\tau(s + j\omega) + 1} = \frac{1}{\tau s + 1} + j\frac{\tau\omega}{(\tau s + 1)^2 + (\tau\omega)^2} \tag{20}$$

The real part does not contain a dummy term and will not lead to the coupling of DQ-axis currents. The presence of a dummy term in the imaginary part is the fundamental cause of the mutual coupling of D-axis and Q-axis currents. To achieve the complete decoupling of the PWM link, the compensation for this item must be made. Figure 6 presents the control block diagram of its compensation method. The input signals are u_{d1} and u_{q1}, and the output signals are u_{d2} and u_{q2}.

The ideal compensator should be the inverse of the transfer function in the PWM link.

$$C(s) = \frac{1}{G_{PWM}(s)} = (\tau s + 1) + j\tau\omega \tag{21}$$

In the dq coordinate system, this complex compensator is presented in the form of a coupling matrix:

$$\begin{bmatrix} u_{d2} \\ u_{q2} \end{bmatrix} = C(s) \begin{bmatrix} u_{d1} \\ u_{q1} \end{bmatrix} = \begin{bmatrix} \tau s + 1 & -\tau\omega \\ \tau\omega & \tau s + 1 \end{bmatrix} \begin{bmatrix} u_{d1} \\ u_{q1} \end{bmatrix} \tag{22}$$

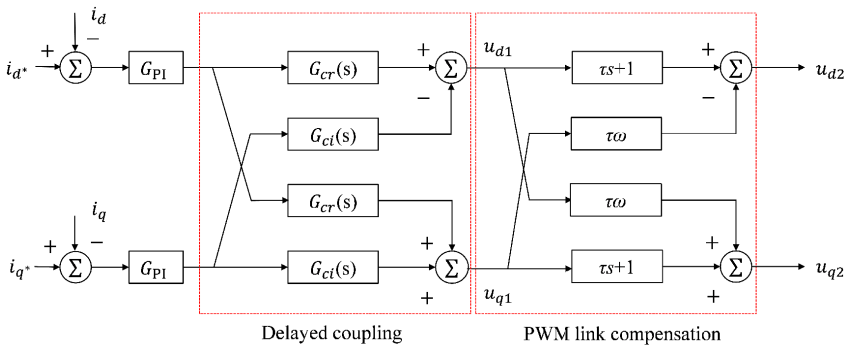

FIGURE 6. Control block diagram of the PWM link compensation method.

TABLE 1. Parameters of PMSM and mechanical load.

Category	Parameter	Value	Unit
PMSM	Stator resistance	0.2	Ω
	d-axis inductance	1.22	mH
	q-axis inductance	1.22	mH
	Permanent magnet flux linkage	0.086	Wb
	Number of pole pairs	4	-
Mechanical Load	Moment of inertia	1.0×10^{-3}	$\mathrm{kg \cdot m^2}$
Inverter & Control	DC-link voltage	36	V
	Switching/Sampling frequency	10	kHz
	Control dead time	2	μs

The diagonal element real part in the compensator matrix is used to compensate for the inherent amplitude attenuation and first-order inertial phase lag of the PWM link itself. The non-diagonal elements $-\tau\omega$ and $\tau\omega$ are the key to decoupling. They generate a cross-feedback term proportional to the synchronous frequency ω, which is precisely used to counteract the virtual counter-electromotive force produced by the combined action of the PWM link and the rotation of the coordinate system. This enables the equivalent PWM link transfer function after compensation to become a pure real number and uncoupled delay link, achieving dynamic decoupling of the D-axis and Q-axis.

5. SIMULATION AND EXPERIMENTAL VERIFICATION

To verify the effectiveness of the direct-pass-free three-level inverter based on complex vector control and its decoupling strategy proposed in this paper, this section conducts a comparative analysis through simulation studies and experimental tests in sequence. The simulation was carried out on the Matlab/Simulink platform to preliminarily verify the correctness of the control algorithm. The experiment builds a principle prototype based on the TMS320F28335 controller, aiming to confirm the feasibility of this strategy in the actual system.

5.1. Simulation Verification

The simulation model built includes: the proposed main circuit of a direct-through three-level inverter with a center-tap inductor, a complex coefficient PI current controller, a PWM modulation, and a decoupling compensation module. The key parameters of the system are set as shown in Table 1. These parameters are consistent with those of the subsequent experimental platform to ensure the comparability between the simulation and experiment.

To evaluate the dynamic decoupling performance of the complex coefficient PI controller, a dynamic response test was conducted on the system. Figure 7 shows the simulation waveforms of the inverter output current under the action of the traditional PI controller and complex coefficient PI controller. From top to bottom, they are: three-phase output current, D-axis current, and Q-axis current. When a step command is applied to the D-axis current at 0.15 seconds, the following phenomena can be observed: the D-axis current can quickly and accurately track the changes in the command. The response process rises rapidly, with a smaller overshoot than the conventional PI control, and the adjustment time is shorter, indicating that the current inner loop has excellent tracking performance. When the D-axis current undergoes a sudden change, the Q-axis current remains basically stable with minimal fluctuations, indicating that the coupling effect caused by the change in the D-axis current has been effectively suppressed. During the transient process, the three-phase current has a good sine waveform and no obvious distortion, which indicates that the system has stability during the dynamic process. The above results confirm that compared with the traditional PI controller, the complex coeffi-

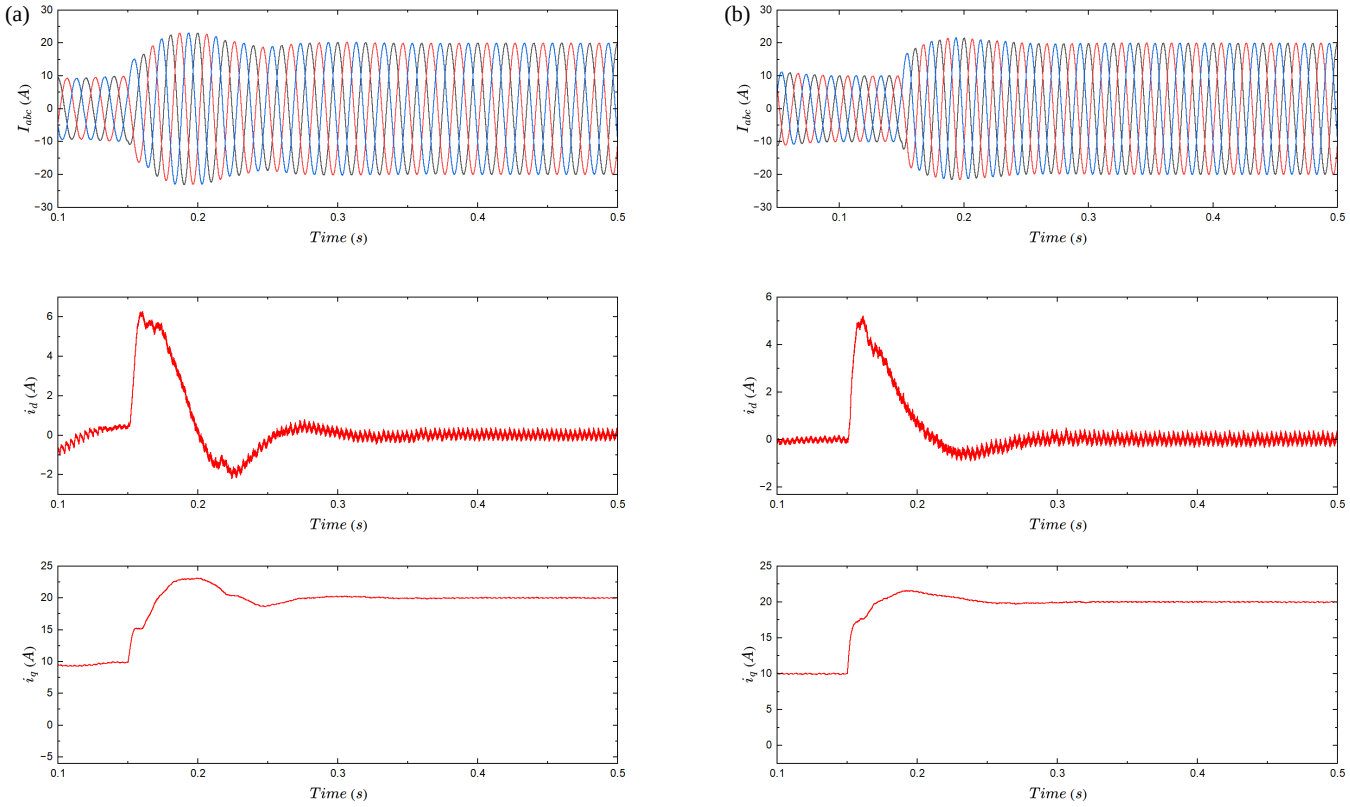

FIGURE 7. Simulation results of the dynamic response of the output terminal current. (a) Conventional Pl control. (b) PI control with complex coefficients.

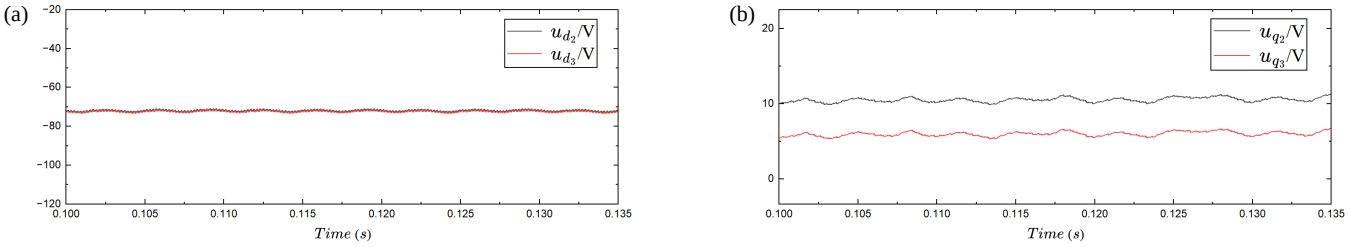

FIGURE 8. Simulation results of PWM modulation decoupling link.

cient PI controller not only achieves rapid current tracking but also effectively realizes the dynamic decoupling of DQ-axis currents.

The PWM modulation process will introduce DQ-axis coupling due to coordinate transformation and computational delay. Figure 8 shows the simulation effect of the feedforward decoupling compensator during steady-state operation. In the figure, u_{d2} and u_{q2} are the voltage instructions output by the PI controller, and u_{d3} and u_{q3} are the final voltage instructions after decoupling compensation and back electromotive force compensation, respectively. Under steady-state conditions, since the rotational speed and current are relatively stable, the decoupling compensation value tends to be constant. It can be seen that the D-axis output u_{d3} superimposes a dynamic compensation quantity on the basis of u_{d2} to counteract the coupling effect of the Q-axis. The Q-axis output u_{q3} superimposes a dynamic compensation quantity on the basis of u_{q2} to counteract the D-axis coupling effect and counter-electromotive force. These compensation quantities will be dynamically adjusted in response to changes in the motor's operating status, thereby achieving decoupled control.

To further evaluate the dynamic performance of the system, a step disturbance is applied to the Q-axis current. Figure 9 shows the dynamic response waveform of the current loop PI controller, from top to bottom: the D-axis and Q-axis current error signals, as well as the PI controller output signals e_d and e_q. At $t = 0.15$ s, the Q-axis current command jumps from 10 A to 20 A. The sudden change in current error causes corresponding changes in ed and eq. These two signals, as important components of the final voltage command, are superimposed with the feedforward decoupling voltage and back electromotive force compensation voltage based on the motor model, jointly forming the voltage reference of the PWM modulation module.

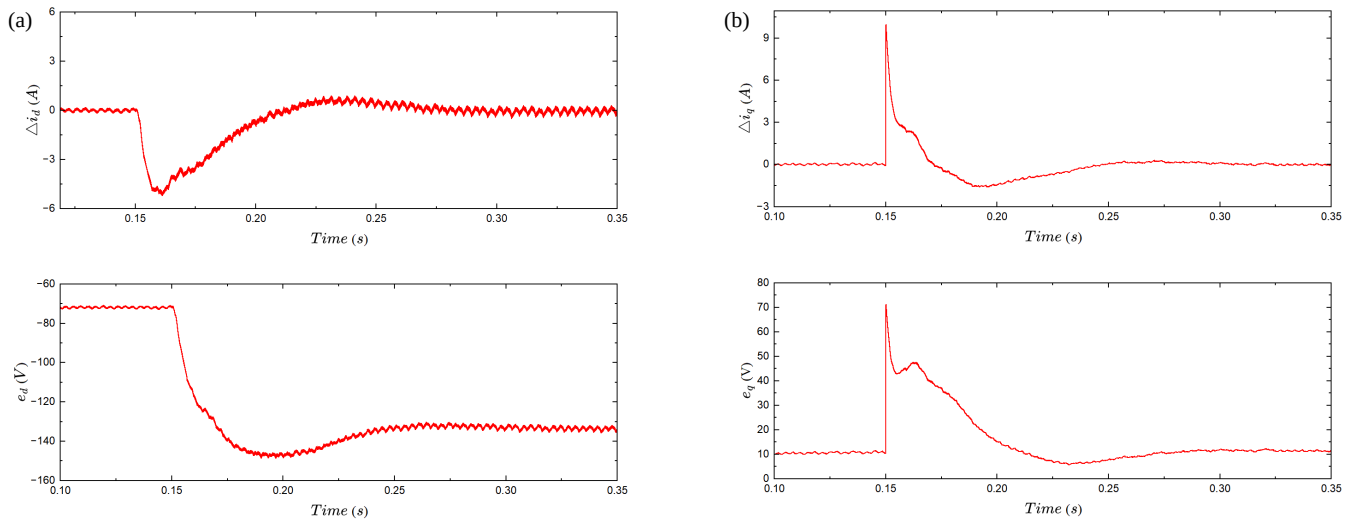

FIGURE 9. Simulation results of PI control link.

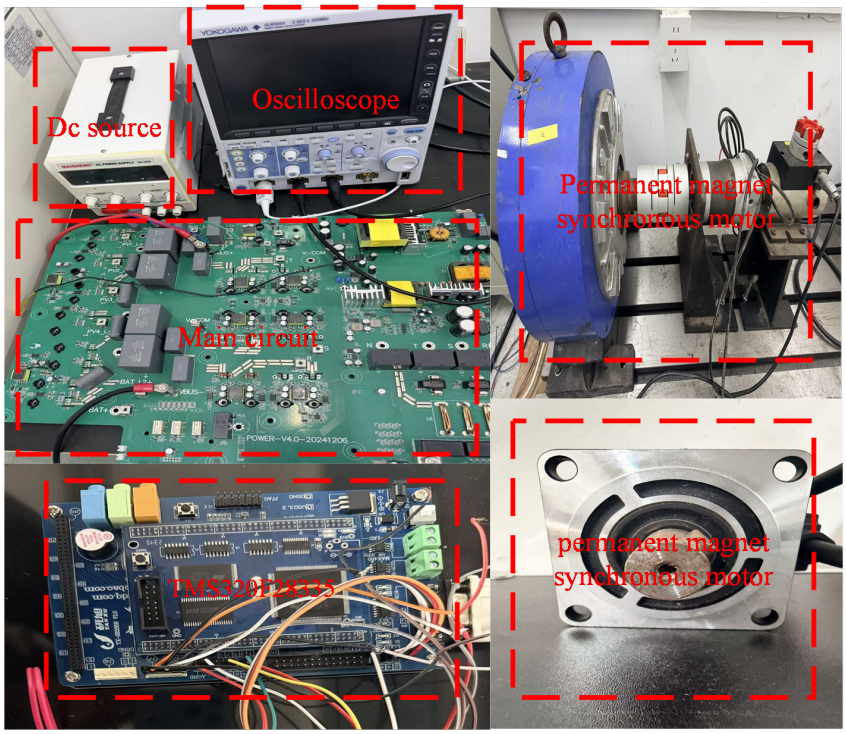

FIGURE 10. Experimental principle prototype.

This result indicates that when the current command changes, the control system rapidly generates new voltage commands through the synergistic effect of PI regulation and feedforward decoupling, ensuring that the current quickly tracks the target value.

5.2. Experimental Verification

To verify the simulation results, an experimental prototype using the TMS320F28335 digital signal processor (DSP) as the core controller was built, as shown in Figure 10. The key module parameters and configurations of the experimental platform are as follows: The main circuit adopts the shoot-through-free three-level topology based on the center-tapped inductor proposed in Section 2 of this paper, with the DC-link voltage set to 36 V. The power switching devices use IGBT modules. The core passive component is the center-tapped inductor, which is a custom-made component. The design of its inductance value meets the dual requirements of output filtering and enables the shoot-through-free operation mechanism. The control system is implemented based on the TMS320F28335 DSP, which executes the proposed complex vector control algorithm in real-time, including complex-coefficient PI regulation and PWM generation. The output phase currents are sampled using

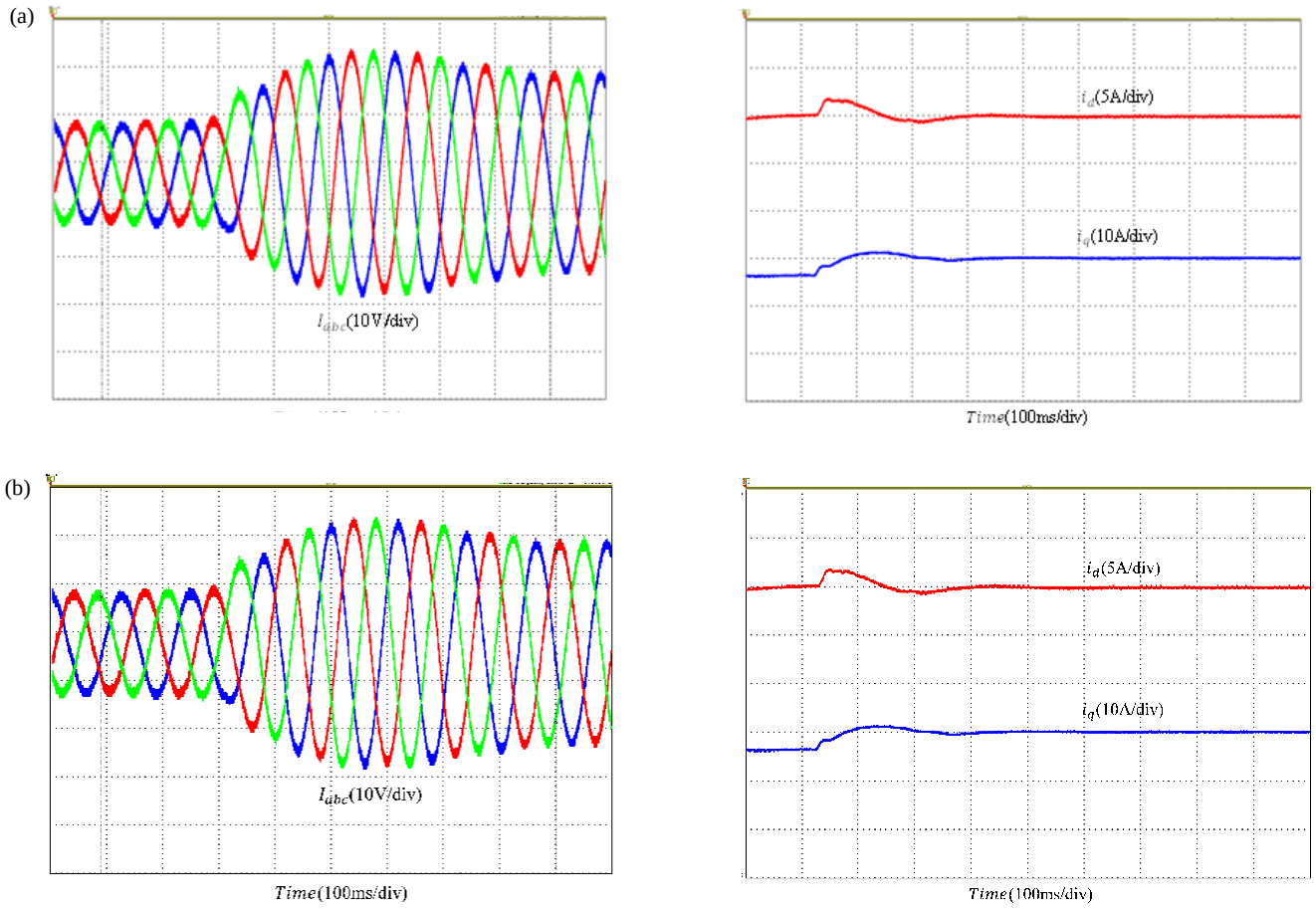

FIGURE 11. Experimental results of dynamic response of inverter output current. (a) Conventional Pl control. (b) PI control with complex coefficients.

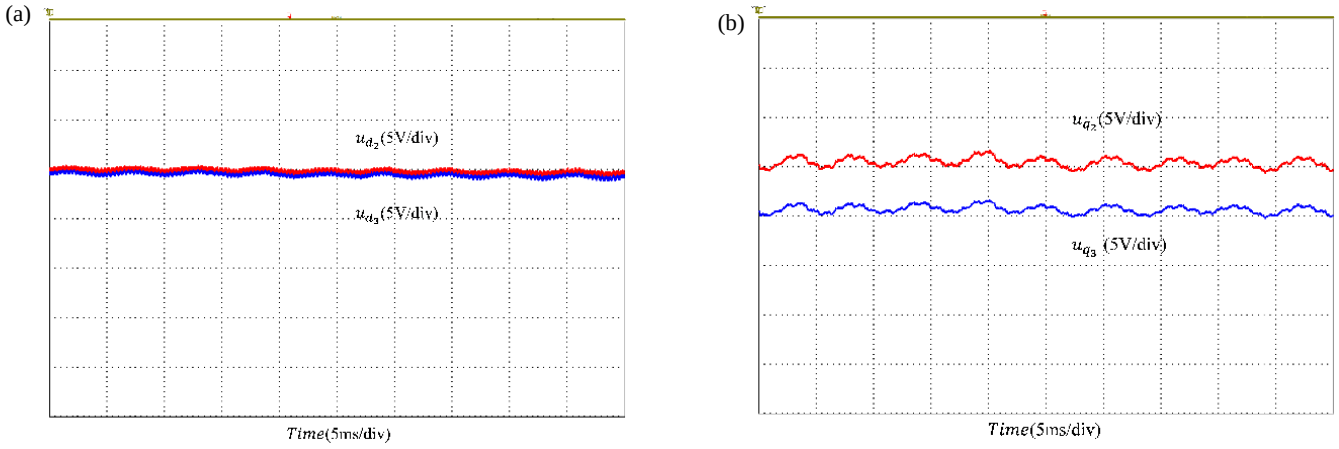

FIGURE 12. Experimental results of PWM modulation decoupling link.

Hall-effect current sensors. For the ease of observation, key internal controller signals, such as u_{d2}, u_{d3}, u_{q2}, and u_{q3}, are output to the oscilloscope via the digital-to-analog (DA) ports of the DSP. The permanent magnet synchronous motor used in the experiment has a stator resistance of 0.2 Ω, d-axis and q-axis inductances of 1.22 mH, a permanent magnet flux linkage of 0.086 Wb, and 4 pole pairs. The load moment of inertia is $1.0 \times 10^{-3}\,\mathrm{kg \cdot m^2}$. These parameters are entirely consistent with those listed in Table 1, ensuring the consistency of simulation and experimental conditions.

In Figure 10, the main circuit board has a relatively large size to provide reasonable layout space for the IGBT module, heat sink, isolated driver circuits, sampling and conditioning circuits, and test interfaces, optimizing heat dissipation, electrical isolation, and measurement convenience. The motor, serv-

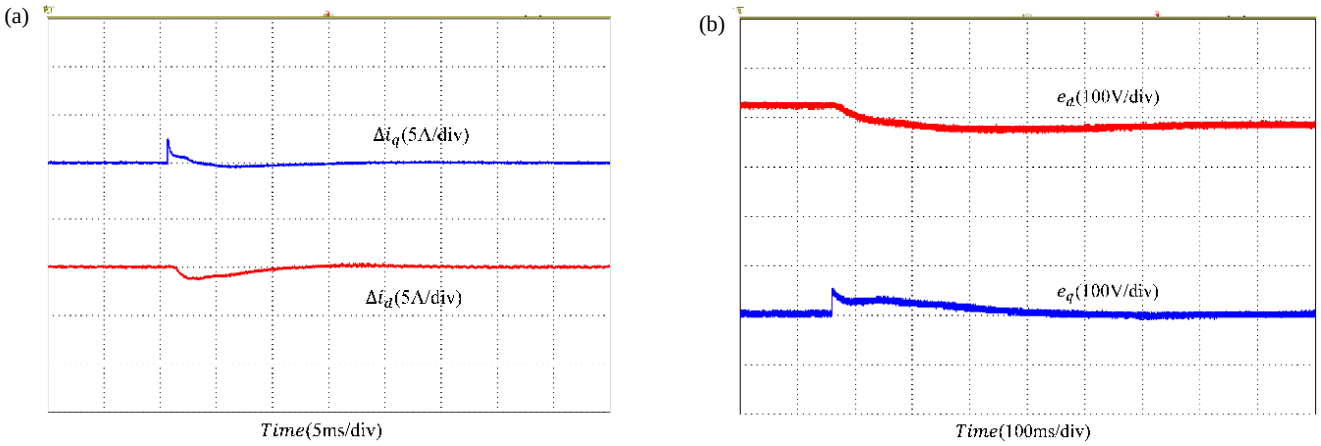

FIGURE 13. Experimental results of PI control link.

ing as an independent load, is connected via cables, resulting in a relatively compact overall structure.

Figure 11 presents the dynamic response experimental results of the DQ-axis current output by the inverter. The reference current suddenly changes from 10 A to 20 A. The DQ-axis current coupling degree with the complex coefficient PI controller is low, and the inverter has good dynamic performance, which proves the effectiveness of the decoupling method proposed in this paper.

Figure 12 presents the experimental results of the PWM modulation decoupling phase, which are consistent with the simulation results. The output signal is a fixed value superimposed on the input signal. Due to the large DC bias between u_{q2} and u_{q3}, in order to observe the waveform more clearly, the DC bias is removed by using the AC mode of the oscilloscope when displaying the wave for the transient response.

Figure 13 presents the experimental results of the PI control link. Similarly, the relevant parameters are output through the DA port of the DSP. Since the set current reference transition time cannot be completely consistent with the simulation, the experimental waveform and simulation waveform are different, but the dynamic change law is the same.

6. CONCLUSION

This paper presents a three-level inverter topology without dead zones, which simultaneously serves the functions of AC side filtering and direct current prevention through an inductor with a center tap. The working principle and control strategy of the inverter are elaborated in detail. By selecting the corresponding switch vector based on the polarity of the output voltage and current, a three-level output is achieved. The proposed inverter and its control strategy have the following advantages:

(1) There is no direct connection problem in the circuit, and there is no need to add dead zones in the drive signal, which avoids the low-order harmonics introduced by dead zones and improves the output power quality.

(2) The concept of complex vectors was introduced; a full-frequency domain model of three-phase inverters was established; and the reasons for the coupling of DQ-axis currents were analyzed based on the response characteristics within the full-frequency domain.

(3) For the additional poles introduced by coordinate transformation, a complex coefficient PI controller was designed to counteract these poles, thereby enhancing the symmetry of the bilateral frequency-domain response curve.

REFERENCES

[1] Lotfi, A., M. Maalandish, A. Aghaei, A. Samadian, A. Fatholahi, S. H. Hosseini, and M.-H. Khooban, "Novel multilevel inverter topology with low switch count," *International Journal of Emerging Electric Power Systems*, Vol. 25, No. 3, 305–319, 2024.

[2] Ye, M., J. Yao, S. Yu, W. Liu, H. Xia, and T. Chen, "Single-pole LS-PWM modulation strategy for symmetric bidirectional multilevel inverters," *High Voltage Engineering*, Vol. 50, No. 04, 1560–1570, 2024.

[3] Ye, S., X. Zhang, and C. Zhu, "DPWM strategy for T-type three-level inverter considering common-mode voltage reduction and neutral-point voltage balance," *Journal of power supply*, Vol. 22, No. 05, 133–142, 2024.

[4] Marufuzzaman, M., M. B. I. Reaz, M. S. Rahman, and M. A. M. Ali, "Hardware prototyping of an intelligent current dq PI controller for FOC PMSM drive," in *International Conference on Electrical & Computer Engineering (ICECE 2010)*, 86–88, Dhaka, Bangladesh, 2010.

[5] Shi, S., X. Wang, S. Zheng, and F. Xia, "A new diode-clamped multilevel inverter for capacitor voltage balancing," *Progress In Electromagnetics Research M*, Vol. 52, 181–190, 2016.

[6] Singh, A. K. and R. K. Mandal, "A new switched capacitor based multi-level inverter with fewer capacitors," *International Journal of Electronics*, Vol. 110, No. 8, 1393–1407, 2023.

[7] Liu, Z.-H., J. Nie, H.-L. Wei, L. Chen, X.-H. Li, and H.-Q. Zhang, "A newly designed VSC-based current regulator for sensorless control of PMSM considering VSI nonlinearity," *IEEE Journal of Emerging and Selected Topics in Power Electronics*, Vol. 9, No. 4, 4420–4431, 2021.

[8] Chu, Y., M. Zhou, C. Wang, and J. You, "Current harmonic minimum pulse width modulation for three-level inverter," *Electric Machines and Control*, Vol. 28, No. 08, 21–30, 2024.

[9] Meraj, S. T., S. S. Yu, M. S. Rahman, A. A. Arefin, M. S. H. Lipu, and H. Trinh, "A novel extendable multilevel inverter for efficient energy conversion with fewer power components: Configuration and experimental validation," *International Journal of Circuit Theory and Applications*, Vol. 52, No. 6, 2760–2785, 2024.

[10] Ning, J., H. Ben, M. Li, T. Meng, and X. Wang, "High-frequency inverter advanced digital modulation strategy and implementation method considering dead time and switching transient effect," *IEEE Journal of Emerging and Selected Topics in Power Electronics*, Vol. 12, No. 2, 1921–1933, 2024.

[11] Wang, C. and A. Wang, "Research on parameter identification algorithm of permanent magnet synchronous motor considering dead time compensation," *Progress In Electromagnetics Research C*, Vol. 138, 205–218, 2023.

[12] Liu, H., X. Wu, W. Kong, G. Long, H. Lou, Z. Liu, and D. Li, "Dead-time compensation based on current phase estimation for high-frequency cascaded transformer multilevel inverter," *IEEE Journal of Emerging and Selected Topics in Power Electronics*, Vol. 12, No. 4, 3540–3551, 2024.

[13] Cao, Y. and Y. Zhao, "Inverter model analysis and dead time compensation control strategy research," *Journal of Hubei University of Technology*, Vol. 39, No. 2, 76–81,92, 2024 (in Chinese).

[14] Liu, X., Y. Pan, L. Wang, J. Xu, Y. Zhu, and Z. Li, "Model predictive control of permanent magnet synchronous motor based on parameter identification and dead time compensation," *Progress In Electromagnetics Research C*, Vol. 120, 253–263, 2022.

[15] Zhou, H., J. Yang, X. Chen, L. Huang, and M. Dong, "Model predictive control of three-level converter considering dead-zone voltage vector," *Transactions of China Electrotechnical Society*, Vol. 37, No. 20, 5290–5301, 2022.

[16] Ghaderloo, R. A., Y. Shen, C. Singhabahu, R. Resalayyan, and A. Khaligh, "Dead-time compensation method for bus-clamping modulated voltage source inverter," in *2023 IEEE Energy Conversion Congress and Exposition (ECCE)*, 2825–2830, Nashville, TN, USA, 2023.

[17] He, M., P. Xue, P. Liu, Y. Liu, and Y. Miao, "Deadtime compensation and control strategy for middle frequency inverter power supply without current sensor," *Electric Machines and Control*, Vol. 27, No. 10, 171–180, 2023.

[18] Xu, X., F. Wang, C. Wu, and X. Feng, "Research and design of microinverter based on dual buck inverter circuit," *Electrical & Energy Management Technology*, Vol. 66, 50–54, 2017.

[19] Khan, A. A., U. A. Khan, H. F. Ahmed, H. Cha, and S. Ahmed, "Improved NPC inverters without short-circuit and dead-time issues," *IEEE Transactions on Power Electronics*, Vol. 37, No. 2, 2180–2190, 2022.

[20] Furlaneto, R. M., I. Kocar, A. Grilo-Pavani, U. Karaagac, A. Haddadi, and E. Farantatos, "Short circuit network equivalents of systems with inverter-based resources," *Electric Power Systems Research*, Vol. 199, 107314, 2021.

[21] Wu, W., X. Z. Ding, and C. Z. Yan, "Research on control method of current loop decoupling based on complex vector," *Proceedings of the CSEE*, Vol. 37, No. 14, 4184–4191, 2017.

[22] Hong, J. J., Y. D. He, J. Z. Huang, and L. Y. Li, "Current decoupling control of PMSM based on improved complex vector," *Electric Machines and Control*, Vol. 27, No. 6, 106–115, 2023.

[23] Jin, A. J., J. S. Zhang, and S. L. Li, "Predictive current control of PMSM model based on adaptive disturbance observer," *Packaging Engineering*, Vol. 44, No. 23, 171–180, 2023.

[24] Liu, Y., X. Wang, and K. Zhou, "Current deviation decoupling control with a sliding mode observer for permanent magnet synchronous motor," *Transactions of China Electrotechnical Society*, Vol. 35, No. 8, 1642–1652, 2020.

[25] Zheng, X., L. Zhang, X. Liu, Y. He, J. Shi, and C. Wang, "Half-cycle control method of the bidirectional three-phase dual-buck inverter without zero-crossing distortion," *IEEE Journal of Emerging and Selected Topics in Power Electronics*, Vol. 9, No. 2, 2088–2097, 2021.

[26] Fu, X. H., S. D. Gu, and J. X. Xiong, "Review of dq axis current decoupling strategy for permanent magnet synchronous motor," *Proceedings of the CSEE*, Vol. 44, No. 1, 314–331, 2024.

[27] Yepes, A. G., A. Vidal, O. López, and J. Doval-Gandoy, "Evaluation of techniques for cross-coupling decoupling between orthogonal axes in double synchronous reference frame current control," *IEEE Transactions on Industrial Electronics*, Vol. 61, No. 7, 3527–3531, Jul. 2014.

[28] Bao, F., H. Guo, Y. Liu, Z. Zhang, and H. Li, "A strategy for improving the dynamic performance of current loop based on complex vector decoupling," *Micromotors*, Vol. 52, No. 12, 74–80, 2019.

[29] Mao, L., Y. Liang, and X. Wang, "Decoupling and compensation strategy for interior PMSM in transitional region of flux-weakening," *Electric Machines and Control*, Vol. 19, No. 7, 14–20, 2015.

[30] Zhu, H., X. Xiao, and Y. Li, "PI type dynamic decoupling control scheme for PMSM high speed operation," in *2010 Twenty-Fifth Annual IEEE Applied Power Electronics Conference and Exposition (APEC)*, 1736–1739, Palm Springs, CA, USA, February 2010.

[31] Zheng, X., J. Hu, X. Liu, Y. He, W. Li, Y. Zhou, and L. He, "Topology construction, modeling, and control of multi-level inverters without shoot-through problem," *IEEE Transactions on Power Electronics*, Vol. 40, No. 5, 6787–6800, 2025.